A confined–unconfined aquifer model for subglacial hydrology and its application to the North East Greenland Ice Stream

Sebastian Beyer[1,2], Thomas Kleiner[2], Vadym Aizinger[2,3], Martin Rückamp[2], and Angelika Humbert[2,4]

[1]Potsdam Institute for Climate Impact Research, Potsdam, Germany
[2]Alfred Wegener Institute, Helmholtz Centre for Polar and Marine Research, Bremerhaven, Germany
[3]Friedrich–Alexander University Erlangen–Nürnberg, Erlangen, Germany
[4]University of Bremen, Bremen, Germany

Correspondence to: Sebastian Beyer (sebastian.beyer@awi.de)

Abstract. Subglacial hydrology plays an important role in the ice sheet dynamics as it determines the sliding velocity of ice sheets and also drives freshwater into the ocean. Modeling subglacial water has been a challenge for decades, and only recently new approaches have been developed such as representing subglacial channels and thin water sheets by separate layers of variable permeability. We extend this concept by modeling a confined and unconfined aquifer system (CUAS) in
5 a single layer. The advantage of this formulation is that it prevents unphysical values of pressure at reasonable computational cost. We also performed sensitivity tests to investigate the effect of different model parameters. The strongest influence of model parameters was detected in terms governing the opening and closure of channels. Furthermore, we applied the model to the North East Greenland Ice Stream, where an efficient system independent of seasonal input was identified about $500\,\mathrm{km}$ downstream from the ice divide. Using the effective pressure from the hydrology model in the Ice Sheet System Model (ISSM)
10 shows considerable improvements of modeled velocities in the coastal region.

1 Introduction

Subglacial water has been identified as a key component in glacial processes, it is fundamental in driving large ice flow variations over short time periods. Recent studies show considerable progress in modeling these subglacial networks and
15 coupling them to ice models. Water pressure strongly influences basal sliding and can therefore be considered a fundamental control on ice velocity and ice-sheet dynamics.

Generally, two fundamentally different types of drainage are identified: discrete channel / conduit systems and distributed water sheets or thin films. Distributed flow mechanisms are, for example, linked cavities (Lliboutry, 1968), flows through sediment/till (Hubbard et al., 1995), or thin water sheets (Weertman, 1957); those are considered to be an inefficient and slow
20 system to transport water. Channels (Rothlisberger, 1969; Shreve, 1972; Nye, 1976) are seen as discrete single features or arborescent networks. It is assumed that these channelized or efficient drainage systems able to drain large amounts of water

in short time spans are predominant in alpine glaciers and on the margins of Greenland, where substantial amounts of surface melt water are capable of reaching the bed. In the interior of Greenland and also in most parts of Antarctica, the water supply is limited to melt due to the geothermal and frictional heating within the ice – a circumstance favoring distributed systems.

Seasonal variations of ice velocity have been observed and attributed to the evolution of the drainage system switching between an efficient and inefficient state in summer and winter (Bartholomew et al., 2010). For this reason, a new generation of subglacial drainage models has been developed recently that is capable of coupling the two regimes of drainage and reproducing the transition between them (Schoof, 2010; Hewitt et al., 2012; Werder et al., 2013; De Fleurian et al., 2014). While these models produce remarkable results for spontaneously evolving channel networks, it is still a challenge to apply them on continental scale. A comprehensive overview of the various existing and newly emerging glaciological hydrology models is given in Flowers (2015).

Distributed or sheet structures can naturally be well represented using a continuum approach, while channels usually require a secondary framework, where each feature is described explicitly. Water transport in channels is a complex mechanism that depends on the balance of melt and ice creep (Nye, 1976; Rothlisberger, 1969), channel geometry, and network topology. Additionally, the network evolves over time which further complicates modeling of this process. This leads to increased modeling complexity and high computational costs. An exception to this is the work of De Fleurian et al. (2014), where both systems are represented by Darcy flow through separate porous media layers. The layer representing the channels has its parameters (namely permeability and storage) adjusted to exhibit the behavior of an effective system.

We take this idea even further and only use a single layer of Darcy flow with locally adjusted transmissivity of the layer at locations where channels form while, at the same time, accounting for a decrease in storage. This means that we approximate the channel flow as a fast diffusion process similarly to work in De Fleurian et al. (2014); however, a single Darcy flow layer with spatially varying parameters (effective permeability) accounts for both drainage mechanisms. Similar approaches are known to have been applied to modeling of fracture networks in rock Van Siclen (2002). This reduced complexity model does not capture channels individually but represents their effect by changing specific local properties. While this strategy may not help to advance the precise understanding of channel formation processes, it captures the overall behavior and allows to examine the complex interactions on larger spatial and temporal scales.

In addition, we introduce a new Confined–Unconfined Aquifer Scheme (CUAS) that differentiates between confined and unconfined flow in the aquifer (Ehlig and Halepaska, 1976). While the assumption of always saturated – and therefore confined – aquifers may be true for glaciers with large water supply, it does not hold in areas with lower water input. Especially in locations far from the coast, the water supplies are often insufficient to completely fill the aquifer. Ignoring this leads to significant errors in the computed hydraulic potential and unphysical, i.a. negative, water pressure.

Large scale ice flow models often compute the basal velocity using a Weertman-type sliding law, where the inverse of the effective pressure (difference between ice overburden pressure and water pressure) determines the velocity at the base. Low effective pressure leads to high basal velocity. Without subglacial hydrology models, the ice models simply take the ice overburden pressure as effective pressure completely neglecting water pressure. This is a major reason why these models

struggle to represent fast flowing areas such as ice streams. The effective pressure computed by our model can be easily coupled to an ice sheet model and improve results for fast flowing areas.

The following work is structured as follows. In the next section, we present the one-layer model of subglacial aquifer and briefly describe its discretization. In Sect. 3 the model is applied to artificial scenarios, and the sensitivity to model parameters

5 and stability are investigated. In addition, results for seasonal forcing are presented there, and we show how the model evolves over time. Section 4 demonstrates the first application of the proposed methodology to the North East Greenland Ice Stream (NEGIS), which is the only interior ice stream in Greenland. It penetrates far into the Greenland mainland with its onset close to the ice divide, so sliding apparently plays a major role in its dynamics. A short conclusions and outlook section wraps up the present study.

2 Methods

2.1 Confined–Unconfined Aquifer Scheme

The vertically integrated continuity equation in combination with Darcy's law leads to the general *groundwater flow equation* (see e.g. Kolditz et al. (2015)):

$$S\frac{\partial h}{\partial t} = \nabla \cdot (T \nabla h) + Q \tag{1}$$

15 with S the storage coefficient (the volume of water released per unit decline of the hydraulic potential over a unit area), h the hydraulic head (piezometric head), T transmissivity of the porous medium, and Q the source term. For a confined aquifer, $T = Kb$, where K is the hydraulic conductivity, and b is the aquifer thickness. $S = S_s b$ with specific storage S_s given by

$$S_s = \rho_{\mathrm{w}} \omega g \left(\beta_{\mathrm{w}} \frac{\alpha}{\omega} \right) \tag{2}$$

with material parameters for the porous medium (porosity ω, compressibility α) and water (density ρ_{w}, compressibility β_{w}).

20 Usually the transmissivity T is assumed as spatially uniform and isotropic, and the right hand side is written as $Kb\nabla^2 h + Q$.

In order to consider the general form covering both cases (confined and unconfined), we follow Ehlig and Halepaska (1976) and write the general form for the confined–unconfined problem:

$$S_e(h)\frac{\partial h}{\partial t} = \nabla \cdot (T(h) \nabla h) + Q. \tag{3}$$

Now the transmissivity and the storage coefficient depend on the head and are defined as

$$25 \quad T(h) = \begin{cases} Kb, & h \geq b & \text{confined} \\ Kh, & 0 \leq h < b & \text{unconfined} \end{cases} \tag{4}$$

and effective storage coefficient S_e is given by

$$S_e(h) = S_s b + S'(h) \tag{5}$$

with

$$S'(h) = \begin{cases} 0, & b \leq h & \text{confined,} \\ (S_y/d)(b-h), & b-d \leq h < b & \text{transition,} \\ S_y, & 0 \leq h < b-d & \text{unconfined.} \end{cases} \tag{6}$$

This means that as soon as the head sinks below the aquifer height, the system becomes unconfined at this point, and therefore only the saturated section contributes to the transmissivity calculation. Additionally, the mechanism for water release changes from elastic relaxation of the aquifer (confined) to dewatering under the forces of gravity (unconfined). The amount of water that is released from dewatering is described by the specific yield S_y. Since the amount of water released this way is usually orders of magnitudes larger than release from confined aquifer ($S_y \gg S_s b$), it is useful to introduce a gradual transition as in Eq. (6) controlled by a user defined transition parameter d.

Note that the transmissivity is no longer homogeneous making Eq. (3) nonlinear. This fits with our approach to describe the effective system (channels) by locally increasing the permeability. The benefit of this approach is discussed in Sect. 3.2.

Water pressure P_w and effective pressure N are related to hydraulic head as

$$P_w = (h - z_b)\rho_w g \tag{7}$$

and

$$N = P_i - P_w \tag{8}$$

with z_b bedrock height, g acceleration due to gravity, $P_i = \rho_i g H$ the cryostatic ice overburden pressure exerted by ice with thickness H and density ρ_i.
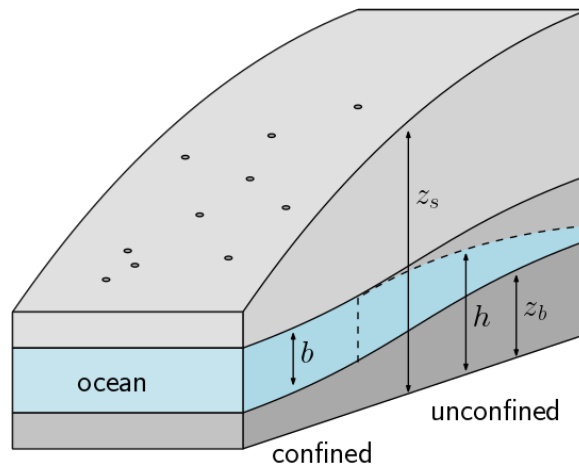
Figure 1. Schematics of the confined–unconfined aquifer scheme and artificial geometry for experiments. Dots on top indicate moulins.

2.2 Opening and closure

Opening and closure of channels is governed by melt at the walls due to the dissipation of heat and the pressure difference between the inside and outside of the channel leading to creep deformation. We follow de Fleurian et al. (2016) in using the classical channel equations from Nye (1976) and Röthlisberger (1972) to scale our transmissivity in order to reproduce this

5   behavior. In contrast to de Fleurian et al. (2016) we do not evolve the aquifer thickness but the conductivity K, which leads to

$$\frac{\partial K}{\partial t} = v_{\text{melt}} + v_{\text{creep}} \tag{9}$$

in which

$$v_{\text{melt}} = \frac{rg\rho_{\text{w}}bK}{\rho_{\text{i}}L}(\nabla h)^2 \tag{10}$$

and

10   $$v_{\text{creep}} = 2An^{-n}|N|^{n-1}NK \tag{11}$$

with L the latent heat, r roughness factor, A the creep rate factor depending on temperature, and n the creep exponent, which we choose as $n = 3$. Depending on the sign of N, creep closure as well as creep opening can occur. Negative effective pressure over prolonged time is usually considered unphysical, and the correct solution to this would be to allow the ice to separate from the bed (see e.g. (Schoof et al., 2012) for a possible solution). However, in the context of our equivalent layer model, Eq. (11)

15   is still applicable because this is how a channel would behave for $N < 0$. In Sect. 3.1, we test the sensitivity of K and N to the magnitudes of r and A.

2.3 Discretization

We discretize the transient flow equation (Eq. (3)) on an equidistant rectangular grid using an explicit forward in time central in space (FTCS) finite-difference approximation. For sake of completeness, we give the equations for a non-equidistant grid

20   here.

For the spatial discretization, we use a second-order central difference scheme (e.g., Ferziger and Perić, 2002) leading to the spatial discretization operator for the head $\mathcal{L}_h$:

$$\mathcal{L}_h = T_{i+\frac{1}{2},j}\frac{h_{i+1,j} - h_{i,j}}{(\Delta_f x)_i(\Delta_c x)_i} - T_{i-\frac{1}{2},j}\frac{h_{i,j} - h_{i-1,j}}{(\Delta_b x)_i(\Delta_c x)_i}$$
$$+ T_{i,j+\frac{1}{2}}\frac{h_{i,j+1} - h_{i,j}}{(\Delta_f y)_j(\Delta_c y)_j} - T_{i,j-\frac{1}{2}}\frac{h_{i,j} - h_{i,j-1}}{(\Delta_b 1)_j(\Delta_c y)_j} + Q \tag{12}$$

25   where half-grid values of T denote harmonic rather than arithmetic averages computed using Eq. (4), where

$$(\Delta_c x)_k = (x_{k+1} - x_{k-1})/2, \tag{13}$$

$$(\Delta_f x)_k = x_{k+1} - x_k, \quad \text{and} \tag{14}$$

$$(\Delta_b x)_k = x_k - x_{k-1} \tag{15}$$

denote central, forward, and backward differences, respectively. Re-writing this more compactly in compass notation

$$\mathcal{L}_h = d_\mathrm{S} h_\mathrm{S} + d_\mathrm{W} h_\mathrm{W} + d_\mathrm{P} h_\mathrm{P} + d_\mathrm{E} h_\mathrm{E} + d_\mathrm{N} h_\mathrm{N} + Q \tag{16}$$

with

$$d_\mathrm{W} = \frac{T_{i-\frac{1}{2},j}}{(\Delta x)_i^2}, \quad d_\mathrm{E} = \frac{T_{i+\frac{1}{2},j}}{(\Delta x)_i^2}, \quad d_\mathrm{S} = \frac{T_{i,j-\frac{1}{2}}}{(\Delta x)_j^2}, \quad d_\mathrm{N} = \frac{T_{i,j+\frac{1}{2}}}{(\Delta x)_j^2},$$

5   and $$d_\mathrm{P} = -(d_\mathrm{W} + d_\mathrm{E} + d_\mathrm{S} + d_\mathrm{N}). \tag{17}$$

We use the explicit Euler method for the time discretization, where the next time step $m+1$ is computed from the previous time step m ($\Delta t = t_{m+1} - t_m$) (using a somewhat sloppy notation)

$$h^{m+1} = h^m + \frac{\Delta t}{S_e} (d_\mathrm{S}^m h_\mathrm{S}^m + d_\mathrm{W}^m h_\mathrm{W}^m$$
$$+ d_\mathrm{P}^m h_\mathrm{P}^m + d_\mathrm{E}^m h_\mathrm{E}^m + d_\mathrm{N}^m h_\mathrm{N}^m - Q^m). \tag{18}$$

10   Conductivity is updated in each time step by Eq. (9):

$$K^{m+1} = K^m + \Delta t \left(v_\mathrm{melt}^m - v_\mathrm{creep}^m \right), \tag{19}$$

where we use a combined forward- backward-difference scheme for the discretization of $(\nabla h)^2$ in Eq. (10):

$$(\nabla h)^2 \qquad \approx \frac{1}{2} \left[\left(\frac{h_{i,j} - h_{i-1,j}}{(\Delta_b x)_i} \right)^2 + \left(\frac{h_{i+1,j} - h_{i,j}}{(\Delta_f x)_i} \right)^2 \right. \tag{20}$$
$$\left. + \left(\frac{h_{i,j} - h_{i,j-1}}{(\Delta_b y)_j} \right)^2 + \left(\frac{h_{i,j+1} - h_{i,j}}{(\Delta_f y)_j} \right)^2 \right].$$

15   Compared to central differences, this stencil is more robust at nodes with large heads caused by moulins.

The time step is chosen sufficiently small that the discretization error is dominated by the spatial discretization. Additionally, we check that the time step is small enough for the unconfined component of the scheme to become active by restarting the time step with a decreased Δt if at any point $h < z_b$.

All variables are co-located on the same grid, but the conductivity K is evaluated at the midpoints between two grid cells
20   using the harmonic mean due to its better representation of conductivity jumps (e.g. at no-flow boundaries).

A big disadvantage of this discrete formulation is that it is not mass-conservative (see, e.g. Celia et al. (1990)). The solution to this is to use a mixed formulation for Darcy flow in which also the Darcy velocity is solved for. We discuss the consequences of this limitation and leave the mixed formulation approach for future work.

3 Experiments with artificial geometries

Testing out equivalent layer model and finding parameters for it is not straightforward because there are no directly comparable physical properties. Moreover, observations and measurements of subglacial processes are in general difficult and sparse. We address this by testing the model with some of the benchmark experiments of the **S**ubglacial **H**ydrology **M**odel **I**nter-comparison **P**roject (shmip.bitbucket.io).

The proposed artificial geometry mimics a land-terminating ice sheet margin measured $100\,\mathrm{km}$ in the x-direction and $20\,\mathrm{km}$ in the y-direction. The bedrock is flat ($z_b(x,y) = 0\,\mathrm{m}$) with the terminus located at $x = 0$ while the surface z_s is defined by a square root function $z_s(x,y) = 6\left((x + 5e3)^{1/2} - (5e3)^{1/2}\right) + 1$. Here, we use the SHMIP/B2 setup, which includes 10 moulins with temporally constant supply. Boundary conditions are set to zero influx at the interior boundaries ($y = 0$, $y = 20$, $x = 100$) and zero effective pressure at the terminus. All experiments start with initial conditions that imply zero effective pressure and are run for 50 years to ensure that they reach a steady state.

3.1 Parameter estimation and sensitivity

SHMIP is primarily intended as a qualitative comparison between different subglacial hydrology models, where results from the GlaDS model (Werder et al., 2013) serve as a "common ground". Here, we use it as a basis for initial tuning and study of the sensitivity of our model parameters. The upcoming results from the SHMIP are also the reason why we do not show a comparison to other models in this study but refer to the manuscript in preparation instead.
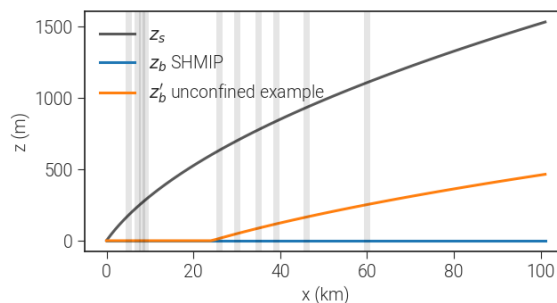
Figure 2. Experiments with artificial geometries. Vertical lines denote moulin positions for SHMIP/B2. The orange line shows the modified bedrock used to illustrate the impact of the confined/unconfined scheme as discussed in Sect. 3.2

In Table 1, we show the physical constants that we use in all setups and runs. The values in the lower half are properties of the porous medium and are only estimated. Since we are dealing with them in the context of the equivalent layer model this is not an issue. Table 2 contains the model parameters in the upper part and the variables computed by the model in the lower part.

We divide the sensitivity analysis into a general block investigating the sensitivity to the amount of water input into moulins, the layer thickness b, the confined / unconfined transition parameter d, model resolution dx (Fig. 3) and a block that examines

Table 1. Physical constants used in the model. We distinguish between well known (upper half) and estimated / uncertain (lower half) parameters.

Name	Definition	Value	Units
L	latent heat of fusion	334	$\mathrm{kJ\,kg^{-1}}$
ρ_{w}	density of water	1000	$\mathrm{kg\,m^{-3}}$
ρ_{i}	density of ice	910	$\mathrm{kg\,m^{-3}}$
n	flow law exponent	3	-
g	gravitational acceleration	9.81	$\mathrm{m\,s^{-2}}$
α	compressibility of water[a]	10^{-8}	$\mathrm{Pa^{-1}}$
β_{w}	compressibility of porous medium[a]	5.04×10^{-10}	$\mathrm{Pa^{-1}}$
ω	porosity[a]	0.4	-
S_s	specific storage (Eq. (5))	$\approx 1 \times 10^{-4}$	$\mathrm{m^{-1}}$
S_y	specific yield	0.4	

[a] Values from De Fleurian et al. (2014)

the parameters directly affecting channel evolution such as channel roughness factor r, creep rate factor A, and bounds for the allowed conductivity K_{min} and K_{max} (Fig. 5). In Table 3, we list values that lead to the best agreement with the SHMIP benchmark experiments and thus are used in the following as the baseline for our sensitivity tests.

In Figs. 3a and b, the model's reaction to different amounts of water input through the moulins is shown. With deactivated
5   conductivity evolution ($K = \mathrm{const.}$, dashed lines), larger water inputs lead to higher water pressure, hence lower effective pressure N. In this case, a moulin input of $18\,\mathrm{m^3\,s^{-1}}$ leads to negative values of N. With activated evolution of K, the conductivity adapts to the water input: as more water enters the system through moulins, the conductivity rises. Vertical gray bars show the location of moulins along the x-axis, and the most significant increase in K occurs directly downstream of a moulin. This happens because the water is transported in this direction leading to increased melt. At the glacier snout ($x = 0$),
10   the ice thickness is at its lowest so almost no creep closure takes place; hence, the conductivity reaches its allowed maximum of $0.5\,\mathrm{m\,s^{-1}}$ for all tested parameter combinations. Significant development of effective drainage is visible for inputs above $2.25\,\mathrm{m^3\,s^{-1}}$ (yellow line). The resulting effective pressure decreases with rising water input as the system becomes more efficient at removing water. Up to ca. $35\,\mathrm{km}$ distance from the snout this results in almost identical values of N for all forcings above $2.25\,\mathrm{m^3\,s^{-1}}$. The system adapts so that it can remove all of the additional water efficiently. In Figs. 3i and j, the two-
15   dimensional distributions of N and K are shown for the baseline parameters; in addition, we detail the temporal development of K in Fig. 4.

"Channels" (indicated by regions of high conductivity) form downstream from moulins and continue straight towards the ocean. The effective pressure drops around water inputs and along the channels. We detect small fluctuations in K directly

Table 2. Model parameters (upper) and variables computed in the model (lower)

Name	Definition	Units
K_{min}	min. conductivity	$\mathrm{m\,s^{-1}}$
K_{max}	max. conductivity	$\mathrm{m\,s^{-1}}$
b	aquifer thickness	m
d	confined / unconfined transition (Eq. (6))	m
Q	water supply	$\mathrm{m\,s^{-1}}$
r	roughness factor	-
A	creep rate factor	$\mathrm{Pa^{-3}\,s^{-1}}$
h	hydraulic head	m
K	hydraulic conductivity	$\mathrm{m\,s^{-1}}$
S	storage	-
S_e	effective storage	-
T	transmissivity	$\mathrm{m^2\,s^{-1}}$
v_{melt}	opening by melt	$\mathrm{m\,s^{-2}}$
v_{creep}	opening/closure by creep	$\mathrm{m^{-2}}$
P_{w}	Water pressure	Pa
P_{i}	Ice pressure	Pa
N	effective pressure	Pa

Table 3. Selected baseline parameters for all experiments unless otherwise noted. These parameters best match the SHMIP targets.

Name	Value	Units
K_{min}	0.003	$\mathrm{m\,s^{-1}}$
K_{max}	0.5	$\mathrm{m\,s^{-1}}$
b	10	m
d	0	m
dx	1000	m
r	1	-
A	5×10^{-25}	$\mathrm{Pa^{-3}\,s^{-1}}$
$Q_{\mathrm{per\ moulin}}$	9	$\mathrm{m^3\,s^{-1}}$

downstream of moulins ("checkerboard patterns") (Figs. 3j and 4); we attribute them to the effects of high conductivity "channels" (giving rise, in turn, to high head gradients that causes aliasing on rather coarse grids used in our simulations). This finding is motivated by the following observations: no fluctuations are seen in the channel corresponding to the rightmost moulin –
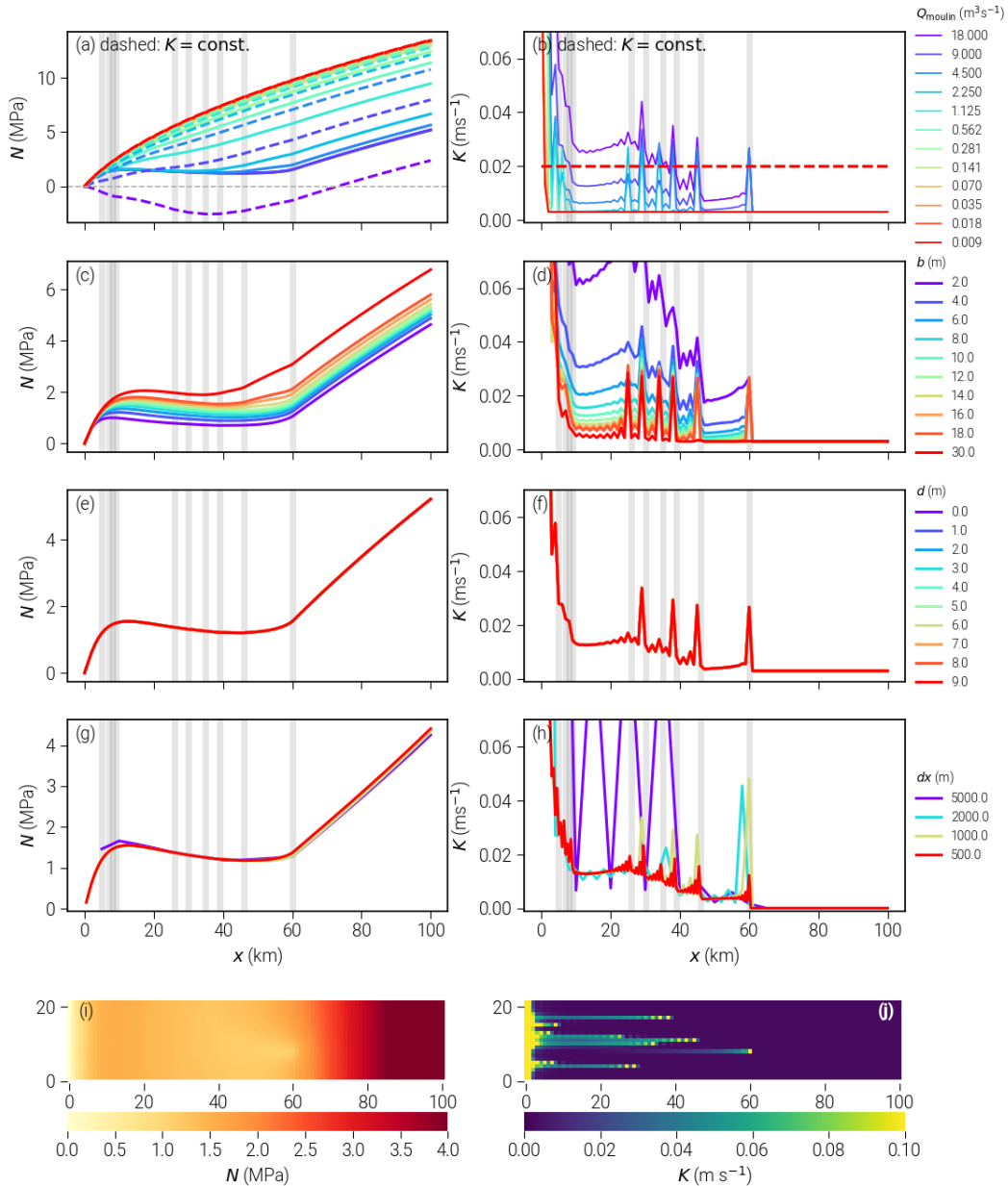
Figure 3. Results from the general sensitivity experiments showing the dependence of N (left) and K (right) on: (a)–(b) Water supply from moulins Q_{moulin} (results for deactivated conductivity evolution are shown using dashed lines), (c)–(d) aquifer layer thickness b, (e)–(f) confined/unconfined transition parameter d, (g)–(h) model resolution dx. Shown values are averaged along the y-axis to represent cross sections at flow lines. Conductivity plots are cut off at $0.06\,\mathrm{m\,s^{-1}}$ to improve visibility of the relevant range. (i) and (j) show the two-dimensional distributions (map view) of the results using the best-fit baseline parameters.
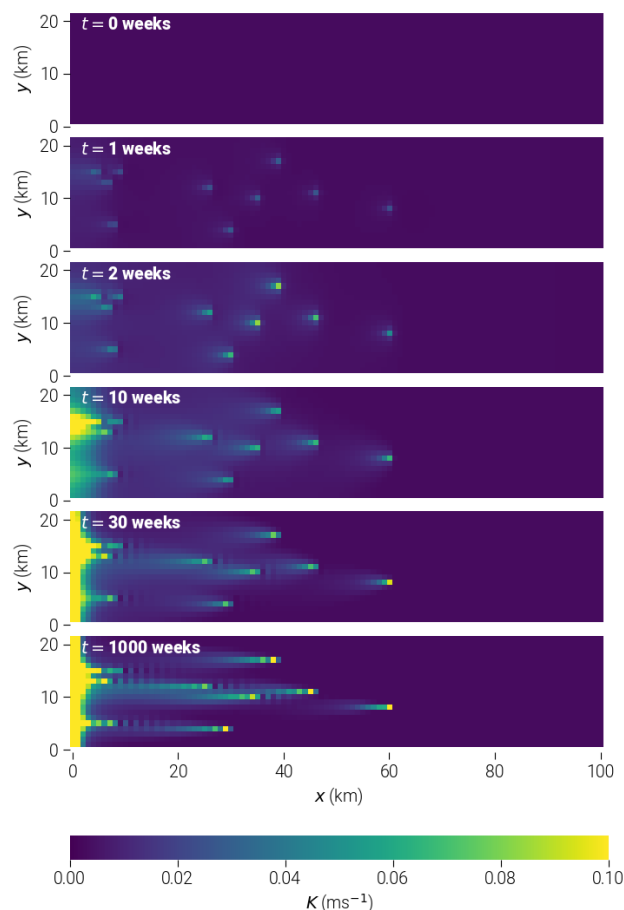
Figure 4. Development of conductivity over time

same as in the results for a single moulin not shown here, the amplitude of fluctuations decreases rapidly with increasing grid resolution (Fig. 3h). In addition, the fluctuations appear to have no significant effect on the resulting pressure distribution.

The layer thickness b directly influences the transmissivity according to Eq. (4). A thicker layer can transport more water out of the system and therefore leads to less water pressure and higher effective pressure (Figs. 3c and d). At the same time, a thinner layer leads to increased water pressure and higher pressure gradients which results in higher v_{melt} and can induce negative effective pressure and creep opening.

The confined–unconfined transition parameter d does not show noticeable effects on the results (Figs. 3e and f) because the experiment has sufficient water input so that all cells are confined in the steady state.

Grid resolution dx has low influence on the pressure distribution but a large effect on the conductivity (Figs. 3g and h). Coarse resolutions lead to large spatial fluctuations of K. Fine resolutions show a weaker checkerboard pattern, which supports our assumption that the pattern results from large gradients in the hydraulic head.
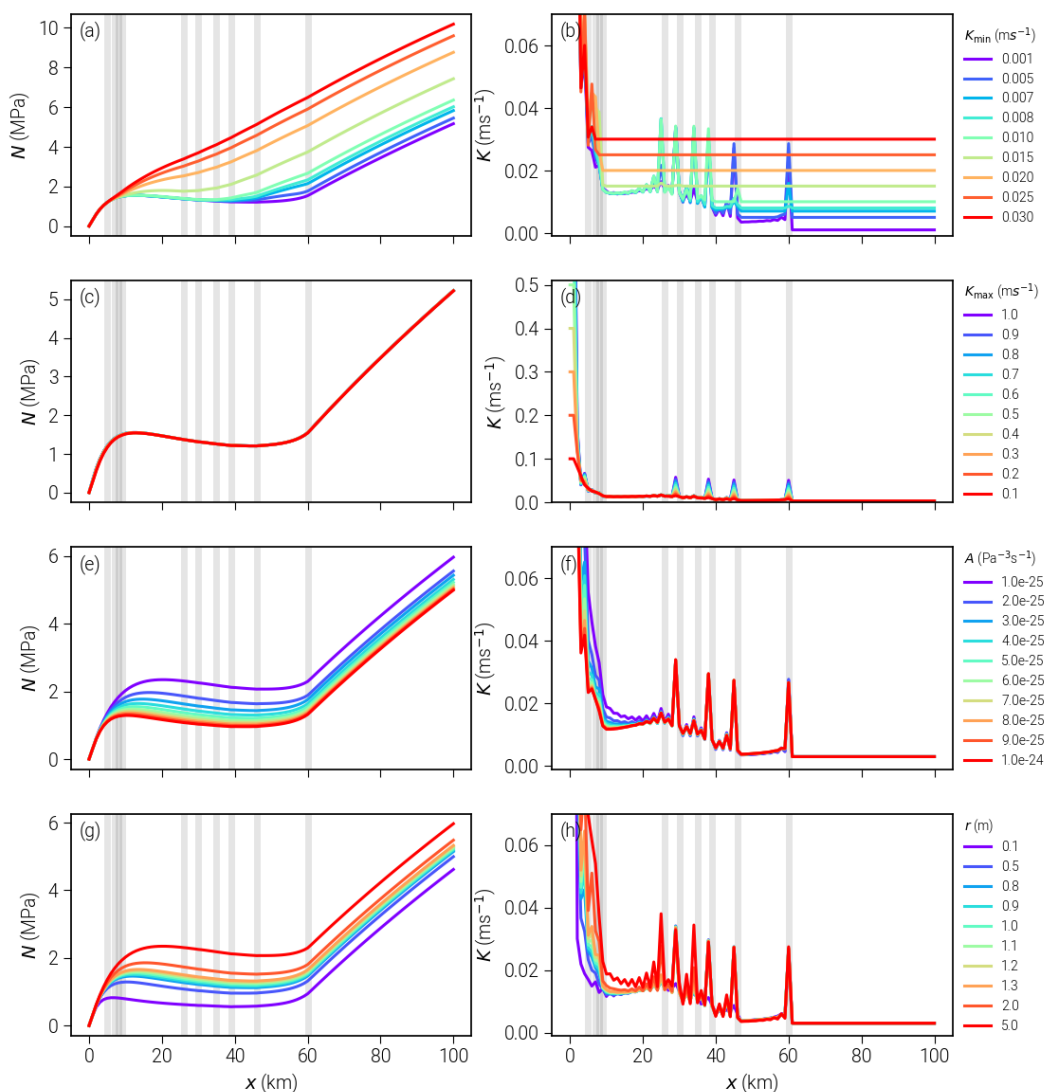
Figure 5. Results from parameters directly related to opening and closure: Limits on the conductivity $K_{\min}$ (panels a and b) and $K_{\max}$ (panels c and d), creep rate factor A (panels e and f) and roughness factor r (panels g and h). Shown values are averaged along the y-axis to represent cross sections at flow lines. Conductivity plots are cut off at $0.06\,\mathrm{ms}^{-1}$ to improve visibility of the relevant range.

In Figs. 5a and b, we show the results for different values of $K_{\min}$. $K_{\min}$ ensures that the system is never completely watertight and determines how much water can pass through independently of the system's current state. Higher values lead to more water transport, lower water pressure, and higher effective pressure. In this experiment, values higher than $0.01\,\mathrm{ms}^{-1}$ show no reactions of K to moulins upstream of $10\,\mathrm{km}$.

$K_{\max}$ (Fig. 5e and f) has no visible impact on the resulting pressure distribution. The differences in K are only large at the snout, where the maximum is always reached because the ice thickness is too low to counteract the melt term. No significant influence on the upstream area has been detected. Rises in conductivity downstream of moulins are amplified with larger $K_{\max}$.

The creep rate factor A determines the "softness" of the ice and therefore effects the creep term in Eq. (9). Larger values of A imply warmer ice; hence, more creep closure (see Figs. 5e and f). Note, that this also effects creep opening if $N < 0$.

The roughness factor r is meant as a measure for small bumps and imperfections, where a rougher channel (larger r) would endure more melt because of the larger contact area and more turbulent mixing. Larger values of r lead to higher conductivity and more water transport resulting in lower P_{w} and higher N.

3.2 The benefit from treating unconfined aquifer

As described above, the confined–unconfined aquifer approach is advantageous in obtaining physically meaningful pressure distributions. In the example illustrated in Fig. 6, we use a slightly modified geometry, where the bedrock rises towards the upstream boundary forming a slab $z_b'(x,y) = \max\left(3((x+5e3)^{1/2} - (5e3)^{1/2}) - 300, 0\right)$. The supply is constant in time and space, and we choose a low value of 7.93e-11 m/s ($\approx$2.5 mm/a) to compare our improved scheme to the simple confined only case. Fig. 6 shows a comparison of the steady state solutions: For the confined-only case, the hydraulic head drops below the bedrock at the upstream region. This results in negative water pressure for these regions. Addressing this by simply limiting the water pressure to zero would result in inconsistencies between the pressure field and the water supply. Our new scheme limits the transmissivity when the head approaches the bedrock and by this means ensures $p_w \geq 0$ in a physically consistent way. Additionally, the unconfined-only solution completely depends on boundary conditions and supply terms, basal topography has no influence in this case.

3.3 Seasonal channel evolution and properties

In order to understand our model's ability to simulate the seasonal evolution of subglacial systems, we selected the setup SHMIP/D and ran it with different values of key model parameters. This experiment does not include any moulins but prescribes a non-uniform spatial distribution of supply instead that also varies seasonally. A simple degree day model with varying temperature parameter $d\Theta$ provides water input rising from the downstream end (lowest elevated) of the glacier towards the higher elevated areas over summer:

$$\Theta(t) = -16\cos\left(2\pi/\mathrm{yr}\ t\right) - 5 + d\Theta \tag{21}$$

$$Q_{\mathrm{dist}}(z_s, t) = \max\left(0, (z_s\mathrm{LR} + \Theta(t))\mathrm{DDF}\right) + Q_{\mathrm{basal}}. \tag{22}$$

Here, $\mathrm{yr} = 31536000\,\mathrm{s}$ denotes the number of seconds per year, $\mathrm{LR} = -0.0075\,\mathrm{Km}^{-1}$ the lapse rate, $\mathrm{DDF} = 0.01/86400\,\mathrm{mK}^{-1}\mathrm{s}^{-1}$ is the degree day factor, and $Q_{basal} = 7.93 \times 10^{-11}\,\mathrm{ms}^{-1}$ is additional basal melt. The resulting seasonal evolution of the supply is shown in Fig.7a. The model is run for 10 years so that a periodic evolution of the hydraulic forcing is generated. Here, we present the result for one parameter set only since the model is not very sensitive in this setup. For the prescribed water supplies, the conductivity only reaches its lower limit $K_{\min}$ for very short periods and the upper limit $K_{\max}$ is never reached
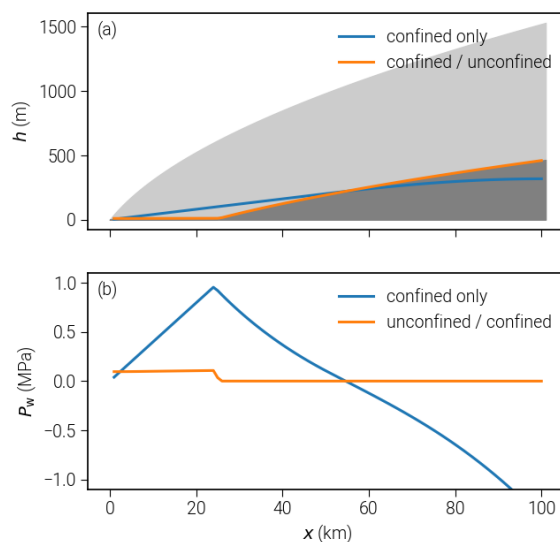
Figure 6. Advantages of using the confined/unconfined aquifer scheme (CUAS): Values of head and water pressure for geometries with non-flat bedrock. (a) Computed head for the confined and combined scheme with ice geometry in the background. In the confined only case, the head is below bedrock. (b) Resulting water pressure, only for the combined scheme the pressure is always non-negative.

at all (apart from the terminus, where it does not have any significant influence on the upstream behavior of the system as we have shown in the previous experiment).

We chose three different locations to present N and K during the season: downstream of the glacier close to the snout, in the center, and at a far upstream location (Figs. 7b–d; the locations are marked in panel g). Shown time series are spatially
5   averaged over these locations with solid lines representing the effective pressure and dashed lines the conductivity.

Water input increases during the summer months, while the corresponding effective pressure drops. With a time lag the conductivity rises in response. Supply develops from downstream towards the upstream end of the glacier over the season so the decline in N at the downstream location (Fig. 7b) is instantaneous when the supply rises, while at the further inland locations (Figs. 7c and d) N reacts later during the year. At the middle location, the drop in N is more intense almost reaching
10   $-5\,\mathrm{MPa}$ for the temperature parameters of 2 and higher. Temperature parameters below -4 show no response at this location. The same applies to the change in conductivity: only the three highest temperatures lead to significant rise of K. Finally, at the upstream position, only for $d\Theta = 4$ and $d\Theta = 2$ the effective pressure drops below zero, while for $d\Theta = 0$ the drop is smaller in magnitude and more prolonged. Conductivity rise is only significant for $d\Theta = 4$ at this location. While the onset and minima of the decline in N strongly depend on the amount and timing of the water input for all values of $d\Theta$, the maximum of K
15   and also the time when N returns to winter conditions is similar. For the downstream position, the maximum conductivity is reached for day 210, and N reaches its background value approximately 25 days later. At the center and upstream positions, this behavior is less pronounced but generally similar.
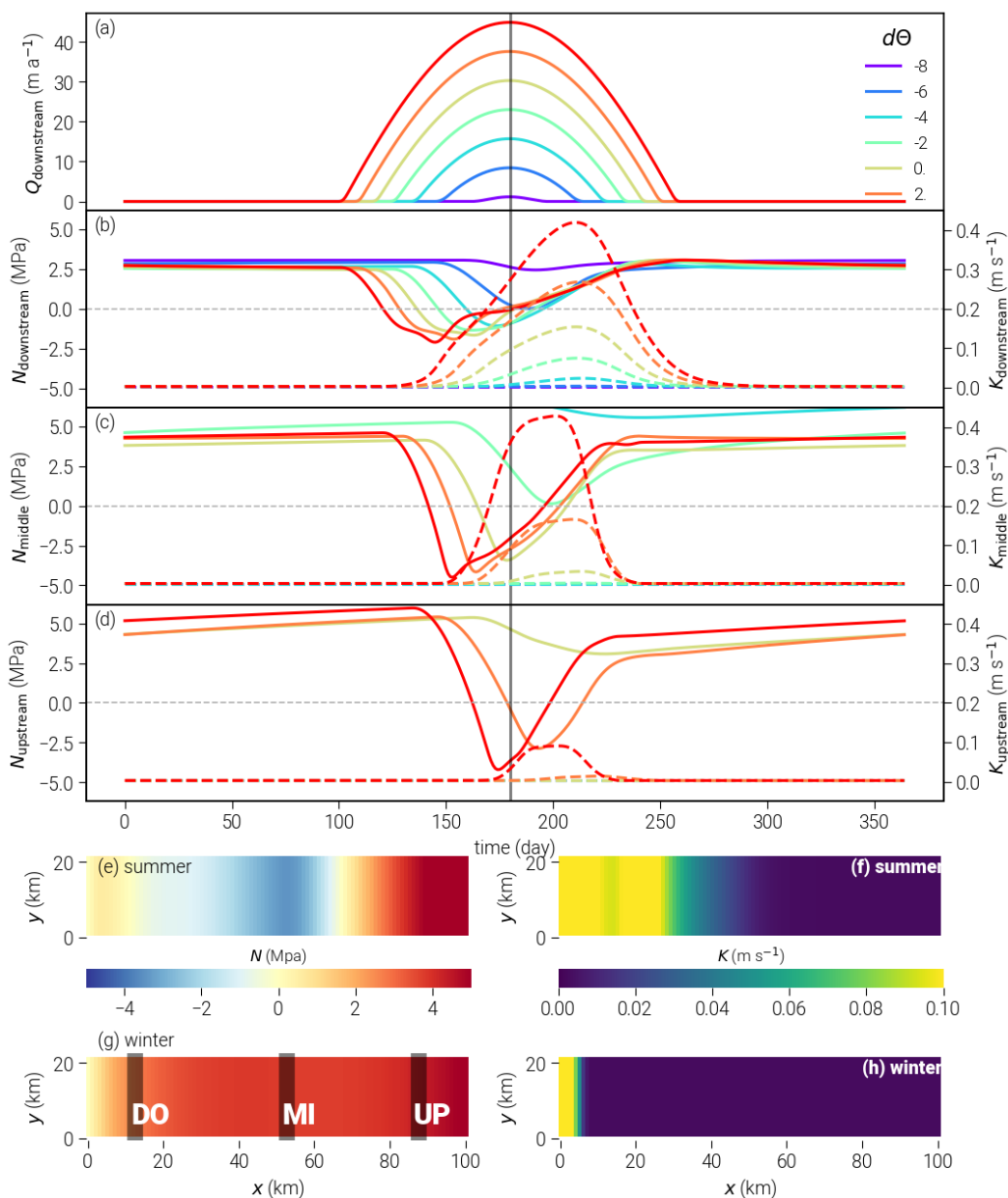
Figure 7. Results for one season of the SHMIP/D experiment. In panels (b)–(d), the left axis (effective pressure) corresponds to the solid lines, while the right axis (conductivity) specifies the values for the dashed lines. The values at the given positions (upstream, middle, downstream) are averaged over the corresponding areas indicated in panel (g). Panels (e)–(h) show two-dimensional distribution maps of $d\Theta = 0$ runs.

The observed behavior is expected and indicates that our model is able to represent the seasonal evolution of the subglacial water system. Increasing water supply over the year leads to rising water pressure and dropping effective pressure. When the

conductivity rises in response, the effective pressure goes up again despite the supply not yet falling again because the more efficient system is able to transport the water away. For the cases where no visible change in K occurs such as $d\Theta = -6$ (blue line in Fig. 7b), the effective pressure directly follows the supply at the terminus, while at the center position ($d\Theta = -2$, cyan line, Fig. 7c), the minimum is offset by the time needed for the supply to reach that location. The maximum in conductivity

5   K is reached later because once the system gets efficient, increased water transport stimulates melting that opens the system even more. This self-reinforcing process is only stopped when enough water is removed and the reduced water flux reduces the melt again. We assume that this leads to similar locations of the conductivity maxima for different $d\Theta$ and the resulting similar reemerging of winter conditions in N.

In this experiment, N becomes negative during the seasonal evolution, which is not physically meaningful. We attribute such

10   behavior to a lack of adjustment of water supply to the state of the system. In reality, the supply from runoff or supraglacial drainage would cease as soon as the pressure in the subglacial water system becomes too high; here we simply continue to pump water into the subglacial system without any feedback. This then leads to negative values of N. It is also consistent with the finding that N becomes negative earlier in the season in cases of higher supply. This deficiency will be addressed in future work.

15   4   Subglacial hydrology of NEGIS, Greenland

The role of subglacial hydrology in the genesis of ice streams in general is not well understood yet. NEGIS is a very distinct feature of the ice sheet dynamics in Greenland; thus, the question about the role of subglacial water in the genesis of NEGIS is critical. The characteristic increase in horizontal velocities becomes apparent about $100\,\mathrm{km}$ downstream from the ice divide (Vallelonga et al., 2014). Further downstream, the ice stream splits into three different branches: the $79°$ North Glacier (79NG),

20   Zacharias Isbrae (ZI), and Storstrømmen. Thus far, large scale ice models have only been able to capture the distinct flow pattern of NEGIS when using data assimilation techniques such as inverting for the basal friction coefficient (see e.g. horizontal velocity fields in Goelzer et al., 2017). It is assumed that most of the surface velocity can be attributed to basal sliding amplified by basal water instead of ice deformation (Joughin et al., 2001). This means that the addition of a subglacial hydrology might have the potential to improve the results considerably. While many glaciers in Greenland have regularly draining supraglacial

25   lakes and run-off driving a seasonality of the flow velocities, little is known about the effect at NEGIS (Hill et al., 2017). Because of this lack of data, to avoid an increased complexity, and to focus on the question if basal melt alone can account for the development of an efficient system, we do not include any seasonal forcing into our experiment.

Our setup includes the major parts of this system. The pressure adjusted basal temperature Θ_{pmp} obtained from PISM (Aschwanden et al., 2016) is utilized to define the modeling region. We assume that for freezing conditions at the base ($T_{\mathrm{pmp}} <$

30    $0.1\,\mathrm{K}$) basal water transport is inhibited and take this as the outline of our model domain. Fig. 8 shows the selected area and PISM basal melt rates used as forcing.

For the ice geometry, we use the data of Morlighem et al. (2014) interpolated on a $1.2\,\mathrm{km}$ grid. Boundary conditions at lateral margins are set to no flux, whereas the termini at grounding lines are defined as Dirichlet boundaries with a prescribed head
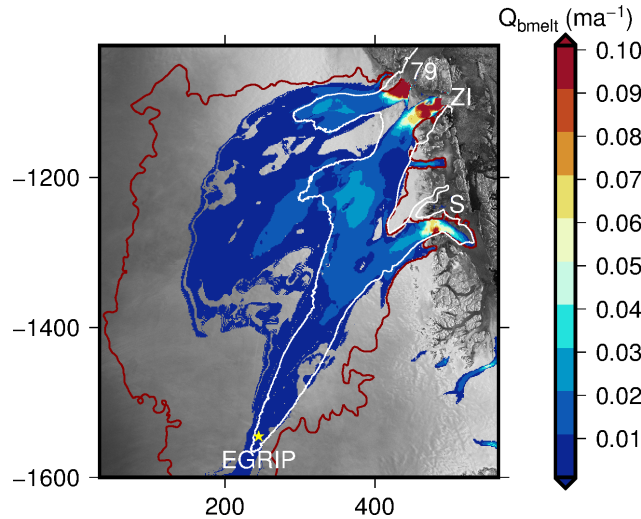
Figure 8. Boundary conditions and forcing for NEGIS experiment. Shown is the basal melt rate from PISM and contour line for $\Theta_{\mathrm{pmp}} = -0.1\,\mathrm{K}$, which is used as model boundary, in red.

that implies an effective pressure of zero. This means that the water pressure at the terminus is equal to the hydrostatic water pressure of the ocean assuming floating condition for the ice at the grounding line. Parameters used for this experiment are the same as those for the previous experiments (Table 3) but with K_{max} reduced to $0.3\,\mathrm{ms}^{-1}$ to speed up the computation. The experiment is run for 50 a to reach steady state. Despite the large number of cells (444×481), computing time for this setup is

5   still reasonable (48 hours on a single core of Intel Xeon Broadwell E5-2697).

The resulting distributions of effective pressure and conductivity are shown in Figs. 9a and b respectively. As expected, effective pressure is highest at the ice divide and decreases towards the glacier termini. Conductivity is low for the majority of the study area with the exception of areas in the vicinity of grounding lines and two distinct areas that touch in between 79NG and ZI. The northern area (marked I in Fig. 9b) is located at the northern branch of 79NG and has no direct connection

10 to the snout. The second area (marked II in Fig. 9b) emerges in the transition zone between the southern branch of 79NG and Zacharias Isbrae and covers an area approximately twice as large as area I with higher values of K. It is connected to the snout of ZI with narrow band of high conductivity cells.

Comparing the effective pressure distribution to the observed velocity (Rignot and Mouginot, 2012) – we chose the $50\,\mathrm{ma}^{-1}$ contour line as indicator of fast flow – we observe coincidence of the fast flowing areas with low effective pressure (below

15 $1\,\mathrm{MPa}$) over most of the downstream areas in our study area. Storstrømmen shows slightly higher effective pressure than 79NG and ZI, which is in accordance with lower observed horizontal velocities for that glacier (Joughin et al., 2010). At the onset of the NEGIS, the effective pressure is high, and no relationship to the flow velocity can be observed.

To further examine the possible influence of our hydrology model to basal sliding we look at the impact on the sliding law. Usually the effective pressure is assumed to simply be the reduced ice overburden pressure N_{HUY} (Huybrechts, 1990).

Therefore, we show the quotient of the inverse of effective pressure in CUAS N_{CUAS}^{-1} and H_{HUY}^{-1} in Fig. 9c. This demonstrates where the application of our hydrology model would increase basal velocities.

In order to demonstrate the effect of the modeled subglacial hydrology system on the NEGIS ice flow, we setup a simple, one-way coupling to an ice flow model. Here, we use the Ice Sheet System Model (ISSM, Larour et al., 2012), an open source finite element flow model appropriate for continental scale and outlet glacier applications (Bondzio et al., 2017; Morlighem et al., 2016). The modeling domain covers the grounded part of the whole NEGIS drainage basin. The ice flow is approximated with the Shelfy-Stream Approximation (SStA) within a 2D plan-view model, which is appropriate for fast flowing ice. As we use the SStA we do not perform a thermo-mechanical coupling but prescribe a depth-averaged hardness factor in Glens flow law. Model calculations are performed on an unstructured finite element grid with a high resolution of $1\,\mathrm{km}$ in fast flow regions and coarse resolution of $20\,\mathrm{km}$ in the interior. The basal drag $\boldsymbol{\tau}_b$ is written in a Coulomb-like friction law:

$$\boldsymbol{\tau}_b = -k^2 N \mathbf{v}_b, \tag{23}$$

where $\mathbf{v}_b$ is the basal velocity vector tangential to the glacier base, N the effective pressure, and k^2 a positive constant. We run two different scenarios, where (1) the effective pressure is parametrized as the reduced ice overburden pressure, $N = N_{\mathrm{HUY}}$, and (2) the effective pressure distribution is taken from the hydrological model at steady state, $N = N_{\mathrm{CUAS}}$. The value of k^2 is tuned in order to have ice velocities of approximately $1500\,\mathrm{ma^{-1}}$ at the grounding line at the 79NG. For both scenarios the value of k^2 is $0.1\,\mathrm{sm^{-1}}$. The results for both scenarios are shown in Fig. 10a and c, respectively. Additionally, we show the observed velocities (Fig. 10d, Rignot and Mouginot, 2012) and the PISM surface velocities (Fig. 10b, Aschwanden et al., 2016). Note that the latter is a PISM model output on a regular grid interpolated to the unstructured ISSM grid.

Velocities computed with the reduced ice overburden pressure are generally too slow and do not resemble the structure of the fast flowing branches at all. The result from PISM shows distinct branches for the different glaciers, which display a relatively sharp separation from the surrounding area. Note, that PISM also uses a basal hydrology model as described in Bueler and van Pelt (2015). Velocities are slightly lower than observed velocities, especially for Zacharias Isbrae and in the area, where ZI and 79NG are closest. In the upper part towards the ice divide, the ice stream structure is not visible in the velocities. The ISSM model using effective pressure computed by CUAS produces high velocities towards the ocean that closely resemble N. The transition between the ice streams and the surrounding ice is poorly reproduced. While the stream structure is way too diffused, the velocity magnitude for the glaciers appears reasonable. The inland part is similar to observed velocities but – as in the PISM simulation – the upper part where NEGIS is initiated is not present. The onset of NEGIS is thought to be controlled by high local anomalies in the geothermal flux (Fahnestock et al., 2001), which PISM currently does not account for. Higher geothermal flux would lead to more basal melt, hence, water supply in the hydrology model. However, the consequences for the modeled effective pressure would require further experiments which are not in the scope of this paper.

We find it impressive that even without extensive tuning, we can considerably improve the velocity field in ISSM by our simple one-way coupling to the hydrology model. However, the results in this section are to be understood not as a thorough study of the NEGIS, but as a first application of the model to a real geometry. A complete study requires extended observations in order to determine the optimal model parameters. However, we are confident that our results represent the general aspects of

the hydrological system at NEGIS. Based on our sensitivity and seasonal experiments (Sect. 3.1 and Sect. 3.3) we expect the high-conductivity-areas to be a stable feature, which would extend or retract depending on the chosen values of the melt and creep parametrizations but not change their location. Available supply plays a more important role here, and we assume that different basal melt distributions – or the addition of surface melt – might considerably change the position and the extent of

5 the efficient system and, therefore, the effective pressure distribution as we can be seen in Sect. 3.3.

The onset of NEGIS is not well reproduced in the PISM simulation as well as in our ISSM result. Since the ice is slow in the PISM results in that area, basal melt rates are low, and, since we use these as input in our hydrology model, it is expected that our model computes low water pressure here. This decisively illustrates the importance of having a real two-way coupling between the ice model and the basal hydrology model in order to obtain good results. These results could then in turn be used

10 to guide further optimization of the modeling parameters in our hydrology model in the future.

5   Conclusions

We present the first equivalent aquifer layer model for subglacial hydrology that includes the treatment of unconfined water flow. It uses only a single water layer with adaptive conductivity. Since extensive observations of the subglacial system are rare, its relative simplicity and empirical nature can be an advantage.

15 We find strong model sensitivity to the lower limit of conductivity $K_{\min}$, grid spacing dx, and the parametrization of melt v_{melt} and creep v_{creep}, while the sensitivity to the upper limit of conductivity $K_{\max}$ and the confined–unconfined transition parameter d is low. Our model robustly reproduces the seasonal cycle with the development and restitution of the effective system over the year.

In our NEGIS experiments, we find the presence of a partial efficient system for winter conditions. The distribution of

20 effective pressure broadly agrees with observed velocities, while the upstream part is not represented correctly. When coupled to ISSM, our hydrology model notably improves computed velocities.

A number of aspects of the proposed model can be further developed; those include improved parametrizations of several physical mechanisms (e.g. adding feedback for between pressure and water supplies), changing scalar conductivity (and thus also the permeability) coefficient to a tensor to better represent the channel anisotropy, and, last but not least, transition to

25 a mixed formulation of the Darcy equation discretized on an unstructured mesh in order to preserve mass conservation and improve computational efficiency.

Competing interests.   The authors declare that they have no conflict of interest.

Acknowledgements. This work is part of the GreenRISE project, a project funded by Leibniz-Gemeinschaft: WGL Pakt für Forschung SAW-2014-PIK-1. We kindly acknowledge the efforts of Basil de Fleurian und Mauro Werder who were designing and supporting the SHMIP project. We highly benefited from their well developed test geometries and fruitful discussions not only at splinter meetings.

We acknowledge A. Aschwanden for providing basal melt rates, temperatures and velocities simulated by PISM. Development of PISM
5   is supported by NASA grants NNX13AM16G, NNX16AQ40G, NNH16ZDA001N and by NSF grants PLR-1644277 and PLR-1603799.

References

Aschwanden, A., Fahnestock, M. A., and Truffer, M.: Complex Greenland outlet glacier flow captured, Nature Communications, 7, https://doi.org/10.1038/ncomms10524, 2016.

Bartholomew, I., Nienow, P., Mair, D., Hubbard, A., King, M. A., and Sole, A.: Seasonal evolution of subglacial drainage and acceleration in a Greenland outlet glacier, Nature Geoscience, 3, 408–411, 2010.

Bondzio, J. H., Morlighem, M., Seroussi, H., Kleiner, T., Rückamp, M., Mouginot, J., Moon, T., Larour, E. Y., and Humbert, A.: The mechanisms behind Jakobshavn Isbræ's acceleration and mass loss: A 3-D thermomechanical model study, Geophysical Research Letters, 44, 6252–6260, https://doi.org/10.1002/2017GL073309, 2017GL073309, 2017.

Bueler, E. and van Pelt, W.: Mass-conserving subglacial hydrology in the Parallel Ice Sheet Model version 0.6, Geoscientific Model Development, 8, 1613–1635, https://doi.org/10.5194/gmd-8-1613-2015, http://www.geosci-model-dev.net/8/1613/2015/, 2015.

Celia, M. A., Bouloutas, E. T., and Zarba, R. L.: A general mass-conservative numerical solution for the unsaturated flow equation, Water Resources Research, 26, 1483–1496, https://doi.org/10.1029/WR026i007p01483, http://dx.doi.org/10.1029/WR026i007p01483, 1990.

De Fleurian, B., Gagliardini, O., Zwinger, T., Durand, G., Le Meur, E., Mair, D., and Raback, P.: A double continuum hydrological model for glacier applications, Cryosphere, 8, 137–153, https://doi.org/10.5194/tc-8-137-2014, 2014.

de Fleurian, B., Morlighem, M., Seroussi, H., Rignot, E., van den Broeke, M. R., Kuipers Munneke, P., Mouginot, J., Smeets, P. C. J. P., and Tedstone, A. J.: A modeling study of the effect of runoff variability on the effective pressure beneath Russell Glacier, West Greenland, Journal of Geophysical Research: Earth Surface, 121, 1834–1848, https://doi.org/10.1002/2016JF003842, http://dx.doi.org/10.1002/2016JF003842, 2016JF003842, 2016.

Ehlig, C. and Halepaska, J. C.: A numerical study of confined-unconfined aquifers including effects of delayed yield and leakage, Water Resources Research, 12, 1175–1183, https://doi.org/10.1029/WR012i006p01175, http://dx.doi.org/10.1029/WR012i006p01175, 1976.

Fahnestock, M., Abdalati, W., Joughin, I., Brozena, J., and Gogineni, P.: High geothermal heat flow, basal melt, and the origin of rapid ice flow in central Greenland, Science, 294, 2338–2342, https://doi.org/10.1126/science.1065370, 2001.

Ferziger, J. H. and Perić, M.: Computational Methods for Fluid Dynamics, Springer, 3rd edn., 2002.

Flowers, G. E.: Modelling water flow under glaciers and ice sheets, Proceedings of the Royal Society A-mathematical Physical and Engineering Sciences, 471, 20140 907, https://doi.org/10.1098/rspa.2014.0907, 2015.

Goelzer, H., Nowicki, S., Edwards, T., Beckley, M., Abe-Ouchi, A., Aschwanden, A., Calov, R., Gagliardini, O., Gillet-Chaulet, F., Golledge, N. R., Gregory, J., Greve, R., Humbert, A., Huybrechts, P., Kennedy, J. H., Larour, E., Lipscomb, W. H., Le clec'h, S., Lee, V., Morlighem, M., Pattyn, F., Payne, A. J., Rodehacke, C., Rückamp, M., Saito, F., Schlegel, N., Seroussi, H., Shepherd, A., Sun, S., van de Wal, R., and Ziemen, F. A.: Design and results of the ice sheet model initialisation experiments initMIP-Greenland: an ISMIP6 intercomparison, The Cryosphere Discussions, 2017, 1–42, https://doi.org/10.5194/tc-2017-129, https://www.the-cryosphere-discuss.net/tc-2017-129/, 2017.

Hewitt, I. J., Schoof, C., and Werder, M. A.: Flotation and free surface flow in a model for subglacial drainage. Part 2. Channel flow, Journal of Fluid Mechanics, 702, 157–187, https://doi.org/10.1017/jfm.2012.166, 2012.

Hill, E. A., Carr, J. R., and Stokes, C. R.: A Review of Recent Changes in Major Marine-Terminating Outlet Glaciers in Northern Greenland, Frontiers in Earth Science, 4, 111, https://doi.org/10.3389/feart.2016.00111, https://www.frontiersin.org/article/10.3389/feart.2016.00111, 2017.

Hubbard, B., Sharp, M., Willis, I., NIELSEN, M. t., and Smart, C.: Borehole water-level variations and the structure of the subglacial hydrological system of Haut Glacier d'Arolla, Valais, Switzerland, Journal of Glaciology, 41, 572–583, 1995.

Huybrechts, P.: A 3-D model for the Antarctic ice sheet: a sensitivity study on the glacial-interglacial contrast, Climate Dynamics, 5, 79–92, 1990.

Joughin, I., Fahnestock, M., MacAyeal, D., Bamber, J. L., and Gogineni, P.: Observation and analysis of ice flow in the largest Greenland ice stream, Journal of Geophysical Research: Atmospheres, 106, 34 021–34 034, 2001.

5   Joughin, I., Smith, B. E., Howat, I. M., Scambos, T., and Moon, T.: Greenland flow variability from ice-sheet-wide velocity mapping, Journal of Glaciology, 56, 415–430, 2010.

Kolditz, O., Shao, H., Wang, W., and Bauer, S., eds.: Thermo-Hydro-Mechanical-Chemical Processes in Fractured Porous Media: Modelling and Benchmarking, Springer, 2015.

Larour, E., Seroussi, H., Morlighem, M., and Rignot, E.: Continental scale, high order, high spatial resolution, ice sheet modeling using the
10   Ice Sheet System Model (ISSM), Journal of Geophysical Research: Earth Surface, 117, https://doi.org/10.1029/2011JF002140, 2012.

Lliboutry, L.: General theory of subglacial cavitation and sliding of temperate glaciers, Journal of Glaciology, 7, 21–58, 1968.

Morlighem, M., Rignot, E., Mouginot, J., Seroussi, H., and Larour, E.: Deeply incised submarine glacial valleys beneath the Greenland ice sheet, Nature Geoscience, 7, 418–422, 2014.

Morlighem, M., Bondzio, J., Seroussi, H., Rignot, E., Larour, E., Humbert, A., and Rebuffi, S.: Modeling of Store Gletscher's
15   calving dynamics, West Greenland, in response to ocean thermal forcing, Geophysical Research Letters, 43, 2659–2666, https://doi.org/10.1002/2016gl067695, 2016.

Nye, J. F.: Water flow in glaciers: Jökulhlaups, tunnels and veins, Journal of Glaciology, 17, 181–207, 1976.

Rignot, E. and Mouginot, J.: Ice flow in Greenland for the international polar year 2008–2009, Geophysical Research Letters, 39, 2012.

Rothlisberger, H.: Water pressure in subglacial channels, in: Union Géodésique et Géophysique Internationale. Association Internationale
20   d'Hydrologie Scientifique. Commission de Neiges et Glaces. Symposium on the hydrology of Glaciers, Cambridge, 7, p. 97, 1969.

Röthlisberger, H.: Water Pressure in Intra- and Subglacial Channels, Journal of Glaciology, 11, 177–203, https://doi.org/10.1017/S0022143000022188, 1972.

Schoof, C.: Ice-sheet acceleration driven by melt supply variability, Nature, 468, 803–806, http://dx.doi.org/10.1038/nature09618, 2010.

Schoof, C., Hewitt, I. J., and Werder, M. A.: Flotation and free surface flow in a model for subglacial drainage. Part 1. Distributed drainage,
25   Journal of Fluid Mechanics, 702, 126–156, 2012.

Shreve, R.: Movement of water in glaciers, Journal of Glaciology, 11, 205–214, 1972.

Vallelonga, P., Christianson, K., Alley, R. B., Anandakrishnan, S., Christian, J. E. M., Dahl-Jensen, D., Gkinis, V., Holme, C., Jacobel, R. W., Karlsson, N. B., Keisling, B. A., Kipfstuhl, S., Kjær, H. A., Kristensen, M. E. L., Muto, A., Peters, L. E., Popp, T., Riverman, K. L., Svensson, A. M., Tibuleac, C., Vinther, B. M., Weng, Y., and Winstrup, M.: Initial results from geophysical surveys and shallow
30   coring of the Northeast Greenland Ice Stream (NEGIS), The Cryosphere, 8, 1275–1287, https://doi.org/10.5194/tc-8-1275-2014, https://www.the-cryosphere.net/8/1275/2014/, 2014.

Van Siclen, C. D.: Equivalent channel network model for permeability and electrical conductivity of fracture networks, Journal of Geophysical Research: Solid Earth, 107, ECV 1–1–ECV 1–10, https://doi.org/10.1029/2000JB000057, http://dx.doi.org/10.1029/2000JB000057, 2002.

35   Weertman, J.: On the sliding of glaciers, J. Glaciol, 3, 33–38, 1957.

Werder, M. A., Hewitt, I. J., Schoof, C. G., and Flowers, G. E.: Modeling channelized and distributed subglacial drainage in two dimensions, Journal of Geophysical Research-earth Surface, 118, 2140–2158, https://doi.org/10.1002/jgrf.20146, 2013.
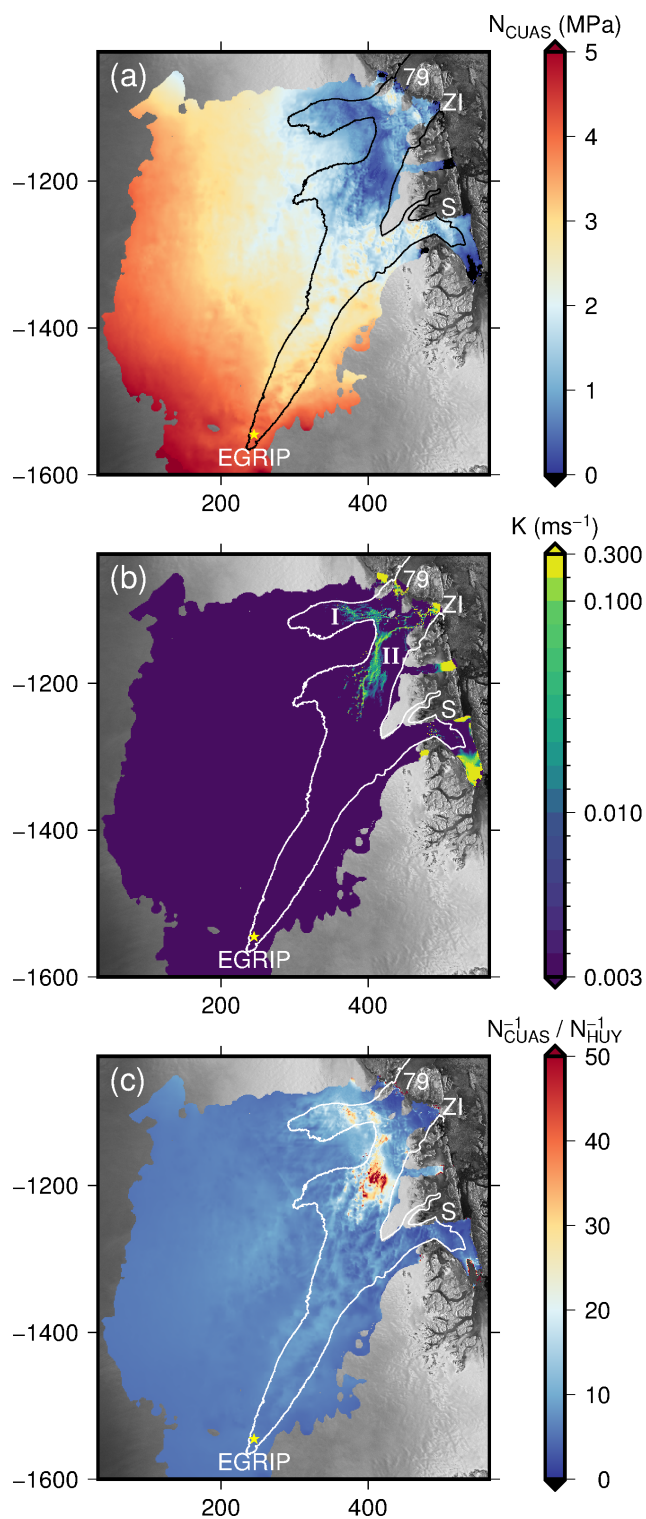
Figure 9. Results for NEGIS region with forcing due to basal melt (PISM), representing winter conditions. White lines indicate the $50\,\mathrm{m\,a^{-1}}$ velocity contour. Panel (a) shows effective pressure N_{CUAS}, (b) conductivity K (logarithmic scale) and (c) shows the quotient of the ice overburden pressure above flotation and the effective pressure computed by CUAS.
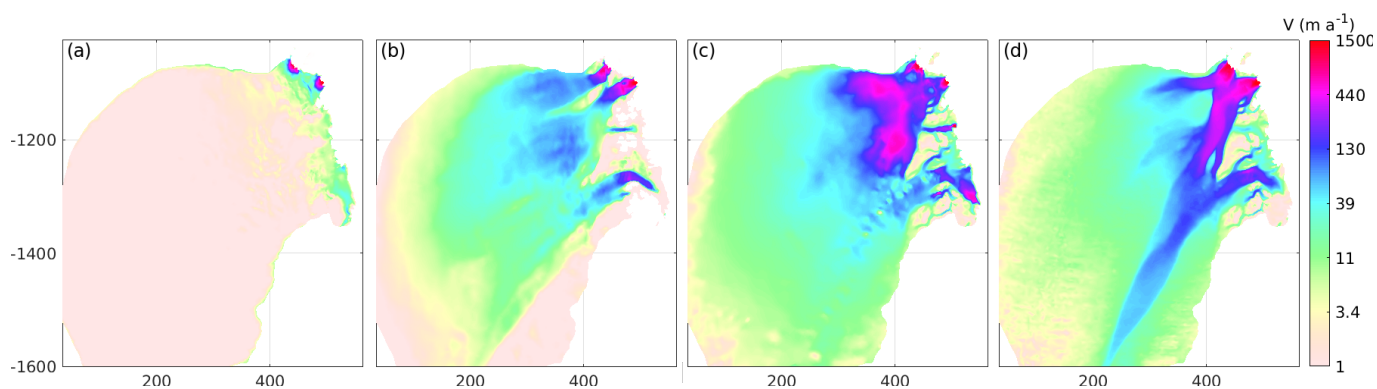
Figure 10. Horizontal surface velocity: ISSM with Reduced ice overburden pressure N_{HUY} (a), PISM result from Aschwanden et al. (2016), interpolated to unstructured ISSM grid (b), ISSM with effective pressure from our hydrology model N_{CUAS} (c) and observed velocities (Rignot and Mouginot, 2012).